IEEE Robotics and Automation Letters (RAL) paper presented at the
2020 IEEE/RSJ International Conference on Intelligent Robots and Systems (IROS)
October 25-29, 2020, Las Vegas, NV, USA (Virtual)

Improving Multirotor Landing Performance on Inclined Surfaces Using Reverse Thrust

John Bass[1] and Alexis Lussier Desbiens[1]

***Abstract*— Conventional multirotors are unable to land on inclined surfaces without specialized suspensions and adhesion devices. With the development of a bidirectional rotor, landing maneuvers could benefit from rapid thrust reversal, which would increase the landing envelope without involving the addition of heavy and complex landing gears or reduction of payload capacity. This article presents a model designed to accurately simulate quadrotor landings, the behavior of their stiff landing gear, and the limitations of bidirectional rotors. The model was validated using experimental results on both low-friction and high-friction surfaces, and was then used to test multiple landing algorithms over a wide range of touchdown velocities and slope inclinations to explore the benefits of reverse thrust. It is shown that thrust reversal can nearly double the maximum inclination on which a quadrotor can land and can also allow high vertical velocity landings.**

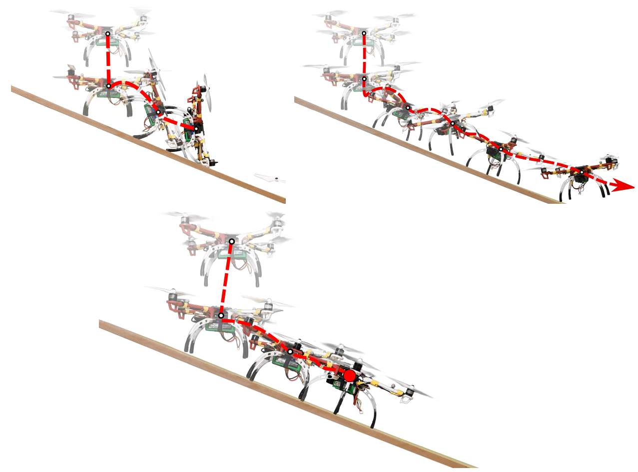

Fig. 1. Conventional quadrotor flipping over during landing on a 25° plane (top left), failing to land due to indefinite bouncing (top right), and successfully landing using the reverse thrust strategy presented in this paper (bottom).

I. INTRODUCTION

The use of uninhabited aerial vehicles (UAVs) for civil applications has increased in recent years, as they are becoming more available, versatile, and safer to fly. However, the vast majority of commercial multirotors have limited landing envelopes and are recommended for landing only on flat horizontal surfaces. Inclined surfaces are likely to cause the UAV to flip over because of the thrust redirection and the UAV's stiff suspension, as shown in Fig. 1. Furthermore, typical flight controllers are programmed to leave their motors running as long as motion is detected, which could lead to continuous motion down small inclines. Newer multirotors are equipped with downward-facing vision sensors, which help them find suitable landing areas during automated landings [1]. Increasing the landing envelope of multirotors could open the door to new applications by increasing the number of possible landing zones or situations; in residential areas, for example, it could allow landing on slanted roofs.

Recent work has focused on developing perching strategies for small aerial robots, as seen in [2]. To remain perched on steeply inclined and vertical surfaces, these use passive methods of adhesion like microspines [3] and dry adhesives [4]. Researchers have also explored using multirotor's agility to create highly dynamic maneuvers for landing and sticking on inclined surfaces [5]. In another study, small onboard lasers and cameras were used to measure a landing area's inclination [6] and a slow (~0.3 m/s) approach trajectory was generated to land. However, most of these multirotors used in this area of research have a relatively low center of gravity, which facilitates the landing maneuver, but reduces payload capacity. Moreover, slow approaches (<0.4 m/s) have the further disadvantage of making the multirotor more susceptible to disturbances during the final approach, such as gusts of wind. Others have installed additional rotors to actuate the horizontal axes [7]. Such a drone is capable of hovering while inclined at 15° and can land on 30° inclinations. Similarly, the development of bidirectional motor controllers has encouraged investigation of omni-directional multirotors [8], [9]. These UAVs use sets of orthogonally placed bidirectional rotors to actuate every degree of freedom, enabling them to fly in any orientation—at the expense of reduced propulsive efficiency, payload capacity, and flight time.

Designing complex landing gears, maneuvers, and multirotor architectures can allow a multirotor to land on steep slopes and even vertical surfaces, as shown in the literature. Yet there is no example of a simple design that would allow multirotors to land on lightly inclined surfaces (i.e., <45°). This article proposes an approach to landing on inclined surfaces that consists in using bidirectional motors to generate reverse thrust. Bidirectional motors could potentially allow for faster approaches, while reverse thrust could "dampen" the system's rebounds after impact and increase the normal contact force and friction. Such a system would push the limits of existing designs while requiring minimal mechanical modifications and minimal added complexity/weight.

Improvements to landing performance can be character-

This work was supported by the NSERC Canadian Robotics Network.

[1] The authors are with the Createk Design Lab, Université de Sherbrooke, Sherbrooke, J1K 2R1, Canada (john.bass@usherbrooke.ca; alexis.lussier.desbiens@usherbrooke.ca).

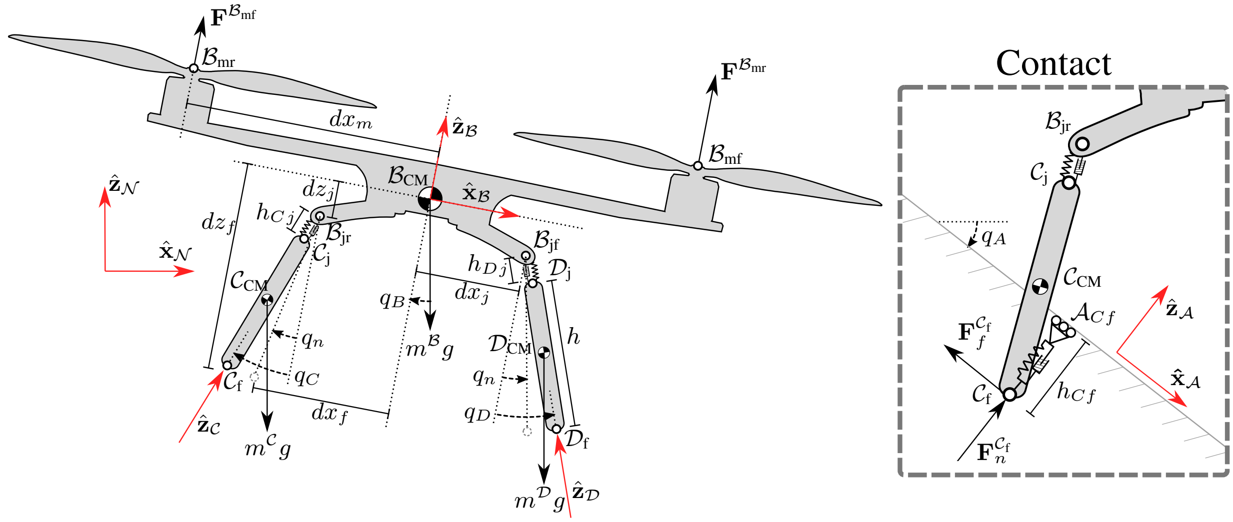

Fig. 2. Diagram of the simplified quadrotor ($\mathcal{B}$), the rear and front legs ($\mathcal{C}$ and $\mathcal{D}$, respectively), the surface ($\mathcal{A}$), the reference frames and the forces included in the dynamic model. Unit vectors $\hat{\mathbf{y}}_{\mathcal{N},\mathcal{A},\mathcal{B},\mathcal{C},\mathcal{D}}$ are all oriented into the XZ plane.

ized by the increase in maximum allowable surface inclination and maximum vertical touchdown velocity, as well by the decrease in the distance and time required for a multirotor to come to rest. In this article, a common DJI F450 quadrotor is chosen to evaluate these potential improvements. To evaluate the effectiveness of reverse-thrust landing strategies, we need a model that can accurately predict the behavior of this quadrotor and its stiff landing gear as it comes into intermittent contact with inclined surfaces. Such a model must allow different landing algorithms to be tested on a wide range of initial conditions. Furthermore, the model must be able to accurately represent the limitations of bidirectional motors, including thrust reversal asymmetry and delays. The different aspects of this model are presented in Section II. Section III then details the designed landing maneuvers and presents the simulated and experimental results.

II. MODEL

A dynamic model was designed to simulate quadrotor landings on a number of inclined surfaces and allow the development of multiple landing strategies. If one assumes the quadrotor is well oriented with the surface prior to the landing maneuver, its movement can be considered to remain generally in a 2D plane (i.e., roll and yaw remain under 10°), which simplifies the model by reducing the number of equations of motion and the number of contact calculations. A multi-body model is used to simulate the behavior of the quadrotor's landing gear that flexes under the landing loads. The model is comprised of three rigid bodies: one quadrotor ($\mathcal{B}$), and two "legs" ($\mathcal{C}$ and $\mathcal{D}$), as presented in Fig. 2. The quadrotor's position in the inertial frame $\mathcal{N}$ is $x_B\hat{\mathbf{x}}_{\mathcal{N}} + z_B\hat{\mathbf{z}}_{\mathcal{N}}$. To approximate the large deformation of the landing gear, even at reasonable touchdown velocities (~0.6 m/s), these rigid segments are connected to the body through both a linear and a torsional spring-damper system. Frames $\mathcal{C}$ and $\mathcal{D}$ are rotated by angles $q_C\hat{\mathbf{y}}_{\mathcal{N}}$ and $-q_D\hat{\mathbf{y}}_{\mathcal{N}}$ respectively relative to frame $\mathcal{B}$ to align the $\hat{\mathbf{z}}_{\mathcal{C}}$ and $\hat{\mathbf{z}}_{\mathcal{D}}$ vectors with the long axis of the legs. At rest, q_C and q_D are equal to q_n. The legs extend at their joint by variable amounts h_{Cj} and h_{Dj}. This section details the rotor thrust model and its validation, as well as the joint model used to estimate the landing gear deflection and the contact/friction models. We then derive the equations of motion, before tuning the model to represent a wide array of landing conditions and validating them through experimental trials.

A. Forces

The various forces modeled are described below.

1) Gravity: The forces of gravity are applied at each body's center of mass ($m^{\mathcal{B}}g$, $m^{\mathcal{C}}g$, $m^{\mathcal{D}}g$).

2) Motor thrust: The sensorless electronic speed controller (ESC) used to control the brushless DC (BLDC) motors involves starting/reversing delays that are critical to the performance and model. Different ESCs were thus compared to select the one with the shortest thrust reversal delay. Transient thrust and torque measurements were acquired using an ATI Mini40 6-axis load-cell at a frequency of 10 kHz. An optical tachometer was also used to measure the angular velocity of the motor. The selected propulsion system consists of four DJI 2312 960Kv motors and 9045 propellers. Fig. 3 compares these ESCs. The DYS XM20A ESC can reverse the rotor thrust in about 400 ms. This ESC runs open-source BLHeli firmware, and by optimizing the parameters, the reversal delay can be reduced to 250 ms. Texas Instruments' Field-Oriented Control ESC, also known as Instaspin [10], was also tested and resulted in reversals of only 220 ms. However, this ESC's performance was inconsistent, requiring up to 750 ms over 50% of the time. The DYS ESC was therefore selected for its reliability.

The thrust forces are applied at two points in the model, $\mathcal{B}_{\mathrm{mf}}$ and $\mathcal{B}_{\mathrm{mr}}$, and are oriented in the $\hat{\mathbf{z}}_{\mathcal{B}}$ direction. The motor dynamics are simulated using a modified model described by [11]. This model is based on Kirchhoff's current law and Newton's second law. To model the reversal delay, the

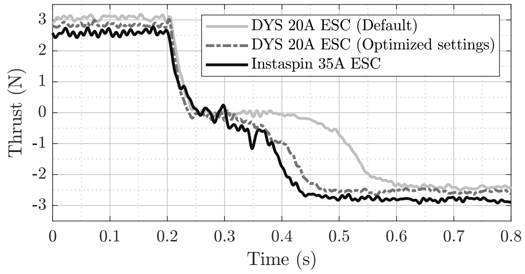

Fig. 3. Measured static thrust response to a reversal command, for different ESCs.

current I_{unsat} is saturated at low speeds in the simulation. The equations for the motor's current I and the motor's angular velocity Ω are thus expressed as

$$I_{unsat}(s) = \frac{V_c - K_v\Omega}{Ls + R}, \tag{1}$$

$$I(s) = \begin{cases} \int_{-I_{sat}}^{I_{sat}} (I_{unsat}), & |\Omega| < \Omega_{min} \text{ and } \frac{d}{dt}|\Omega| > 0 \\ I_{unsat}, & \text{else} \end{cases} \tag{2}$$

$$\Omega(s) = \frac{K_t I - \tau_{aero}}{I^r s + K_d}, \tag{3}$$

where V_c is the command voltage, K_v is the speed constant, L is the motor's armature inductance, R is the armature's resistance, K_t is the torque constant, τ_{aero} is the aerodynamic torque, I^r is the rotor's mass moment of inertia about $\hat{\mathbf{z}}_B$, and K_d is a damping coefficient. The current I is saturated at I_{sat} when $|\Omega|$ is smaller than the value Ω_{min} and when $|\Omega|$ is increasing, as braking is not affected by the ESC's low-speed performance. The command voltage is obtained by using a function $\Omega_0(u)$ to express the relation between the motor's no-load speed and the pulse width modulation (PWM) command duty cycle u, as follows:

$$V_c = \Omega_0(u)/K_v. \tag{4}$$

The linear function $\Omega_0(u)$ is obtained experimentally using the RCbenchmark Series 1585 Thrust Stand. Functions for the rotor thrust $T(\Omega)$ and aerodynamic torque $\tau_{aero}(\Omega)$ were also obtained and were modeled using second-degree polynomial functions (R^2 = 0.998). The effects of axial and radial airspeed are neglected in the model for simplicity.

TABLE I
MOTOR MODEL PARAMETERS

Parameter	Value	Method
k_v (V.s/rad) & k_t (Nm/A)	0.099	Specification
I^r (kg.m^2)	2.7e-5	Measured
R (Ohm)	0.299	GA
L (kg)	0.0038	GA
k_d (N.m.s/rad)	9.2e-9	GA
I_{sat} (A)	0.35	Manual
Ω_{min} (rad/s)	6.3	Manual

Because the motor's parameters are difficult to directly measure, a genetic algorithm (GA) was used to fit the model with experimental data, whereas Ω_{min} and I_{sat} were fitted manually afterwards. We measured the thrust and torque responses to multiple sequential commands. Separate measurements were conducted for the normal and reverse motor directions, to omit the reversal delay. The experimental data was filtered using a tenth-order 100-Hz low-pass Chebyshev Type II filter. The GA varied the selected parameters within a defined range, with the aim of minimizing the average normalized RMS error (NRMSE) between the simulated and measured motor torque and motor speed, over all the trials. Using a population of 200 individuals, Matlab's GA was set to stop after the NRMSE change over 4 generations was less than 0.01%. The GA converged to the values presented in Table I, resulting in an NRMSE of 2.67%. The saturation parameters were then adjusted manually to match the observed reversal delay. A validation sequence containing thrust reversal is presented in Fig. 4.

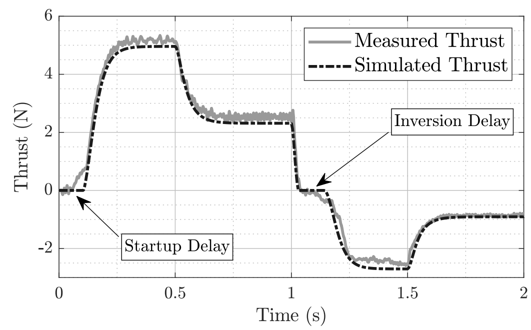

Fig. 4. Measured static thrust as a function of time, responding to different commands every 0.5 s, compared with the model.

3) Body joints: To simulate the legs' deflection, the model includes both a revolute and a linear prismatic joint between each leg and the body. Bending of a leg is represented with the revolute joint [12], whereas the linear joint is added to model buckling. This linear joint is critical to simulate the compression movement of the body when both legs are touching the surface. Both joints are affected by a spring and a damper. The force and moment applied to the body $\mathcal{B}$ by the leg $\mathcal{C}$ through the joint's spring and damper is given by

$$\mathbf{F}^{\mathcal{B}_{\mathrm{jr}}/\mathcal{C}_{\mathrm{j}}} = -\left(k_h h_{Cj} + b_h \dot{h}_{Cj}\right) \cdot \hat{\mathbf{z}}_{\mathcal{C}}, \tag{5}$$

$$\mathbf{M}^{\mathcal{B}/\mathcal{C}} = \left(k_t\left(q_C - q_n\right) + b_t \dot{q}_C\right) \cdot \hat{\mathbf{y}}_{\mathcal{C}}, \tag{6}$$

where k_h and b_h are, respectively, the spring constant and the damping constant of the linear prismatic joint; k_t and b_t are those of the revolute joint, respectively; and q_n is the leg's angle relative to $\mathcal{B}$ at rest. Planar reaction forces between the two bodies are considered at points $\mathcal{B}_{\mathrm{jr}}$ and $\mathcal{B}_{\mathrm{jf}}$ and are solved with the other system states.

B. Contact Model

Contact between the legs and the ground is modeled using an intermittently activated spring-damper on each foot as in [13]. The contact forces $\mathbf{F}_n^{\mathcal{C}_{\mathrm{f}}}$ and $\mathbf{F}_n^{Df}$ act upon points

$\mathcal{C}_\text{f}$ and $\mathcal{D}_\text{f}$ in the direction $\hat{\mathbf{z}}_\mathcal{A}$. For example, the rear foot's contact force is given by the following equation:

$$\mathbf{F}_n^{\mathcal{C}_\text{f}} = \begin{cases} \left(k_s h_{Cf} + b_s \dot{h}_{Cf}\right) \cdot \hat{\mathbf{z}}_\mathcal{A}, & h_{Cf} > 0 \text{ and } \dot{h}_{Cf} > 0 \\ (k_s h_{Cf}) \cdot \hat{\mathbf{z}}_\mathcal{A}, & h_{Cf} > 0 \\ \mathbf{0}, & \text{else} \end{cases} \tag{7}$$

where k_s is the spring's coefficient, b_s is its damping coefficient, and h_{Cf} is $\mathcal{C}_\text{f}$'s penetration. As described below, friction is calculated differently according to whether the surface possesses a low or high coefficient of friction.

1) Low-friction (LF) surfaces: A continuous friction law [14] is used to model friction between the ground and the landing gear to efficiently model both slipping and sticking states. The friction force applied to $\mathcal{C}_\text{f}$ in the $\hat{\mathbf{x}}_\mathcal{A}$ direction is given by

$$F_f^{\mathcal{C}_\text{f}} = \mu_k \left|\mathbf{F}_n^{\mathcal{C}_\text{f}}\right| \frac{\boldsymbol{v}^{\mathcal{C}_\text{f}/\mathcal{A}_{Cf}} \cdot \hat{\mathbf{x}}_\mathcal{A}}{\left|\boldsymbol{v}^{\mathcal{C}_\text{f}/\mathcal{A}_{Cf}} \cdot \hat{\mathbf{x}}_\mathcal{A}\right| + \epsilon_v} \hat{\mathbf{x}}_\mathcal{A}, \tag{8}$$

where μ_k is the coefficient of kinetic friction, $\boldsymbol{v}^{\mathcal{C}_\text{f}/\mathcal{A}_{Cf}}$ is the relative velocity between $\mathcal{C}_\text{f}$ and $\mathcal{A}_{Cf}$ (a point on $\mathcal{A}$ adjacent to $\mathcal{C}_\text{f}$), and ϵ_v is a small number compared to the characteristic value of $\boldsymbol{v}^{\mathcal{C}_\text{f}/\mathcal{A}_{Cf}}$.

2) High-friction (HF) surfaces: The continuous friction law tends to be computationally slow for simulating sticking with higher friction coefficients. Hence, for surfaces with a friction coefficient closer to 1, a hybrid model was designed that let the simulation switch between different models depending on the state of both feet, as shown in Fig. 5. The simulation begins with both feet in flight (the same model as both feet slipping) and can transition to and from a sticking model for each foot and a sticking model for both of them.

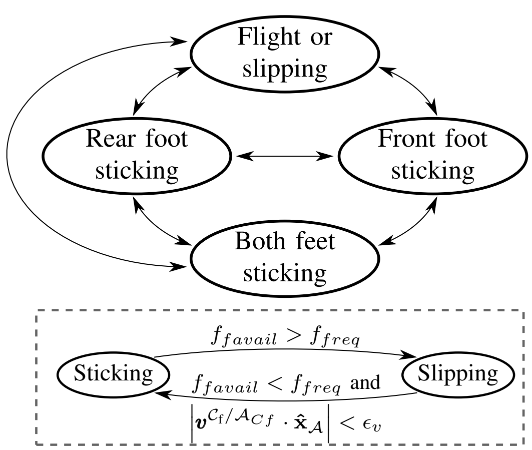

Fig. 5. Transitions of the hybrid model used to simulate contacts with HF surfaces and transition conditions for the rear leg $\mathcal{C}$.

For example, the rear foot $\mathcal{C}_\text{f}$ switches from a slipping state to sticking state when the velocity $\left|\boldsymbol{v}^{\mathcal{C}_\text{f}/\mathcal{A}_{Cf}}\right|$ in the direction $\hat{\mathbf{x}}_\mathcal{A}$ is smaller than a small velocity e_v, and the available friction force f_{favail} is greater than the required friction force f_{freq} to respect the sticking constraint. The reverse transition is done when $f_{favail} < f_{freq}$. The available friction force is calculated differently between the two models:

$$f_{favail} = \begin{cases} \mu_k \left|\mathbf{F}_n^{\mathcal{C}_\text{f}}\right| \dfrac{\boldsymbol{v}^{\mathcal{C}_\text{f}/\mathcal{A}_{Cf}} \cdot \hat{\mathbf{x}}_\mathcal{A}}{\left|\boldsymbol{v}^{\mathcal{C}_\text{f}/\mathcal{A}_{Cf}} \cdot \hat{\mathbf{x}}_\mathcal{A}\right|}, & \text{for slipping,} \\ \mu_s \left|\mathbf{F}_n^{\mathcal{C}_\text{f}}\right|, & \text{for sticking.} \end{cases} \tag{9}$$

This equation includes a combination of Coulomb friction (μ_k) and stiction (μ_s) [15]. The sticking constraint only affects the feet's movement along $\hat{\mathbf{x}}_\mathcal{A}$, because the ground remains compliant throughout the hybrid model, such that

$$\boldsymbol{v}^{\mathcal{C}_\text{f}/\mathcal{A}_{Cf}} \cdot \hat{\mathbf{x}}_\mathcal{A} = 0. \tag{10}$$

This constraint is added to the equations of motion in order to solve for f_{freq} in the sticking model. In the slipping model, f_{favail} is used and f_{freq} is solved separately for the purpose of triggering the transition to sticking.

C. Equations of Motion (EOM)

The system's EOM are obtained to solve for the state variables x_B, z_B, q_B, h_{Cj}, q_C, h_{Dj}, q_D, and their time-derivatives, as well as for both joint reaction forces mentioned in Section II-A.3. A classic Newton-Euler approach was used. Thus,

$$\mathbf{F}^i = m^i * {}^\mathcal{N}\mathbf{a}^{i_\text{CM}}, \tag{11}$$

$$\mathbf{M}^{i/i_\text{CM}} = I_{yy}^{i/i_\text{CM}} * {}^\mathcal{N}\alpha^i, \tag{12}$$

where i represents bodies $\mathcal{B}$, $\mathcal{C}$, and $\mathcal{D}$. Scalar equations are then produced by extracting the $\hat{\mathbf{x}}_\mathcal{N}$ and $\hat{\mathbf{z}}_\mathcal{N}$ components of (11) and the $\hat{\mathbf{y}}_\mathcal{N}$ component of (12). The equations were generated using MotionGenesis [16] and solved in Matlab.

D. Validation

To confirm that the proposed model can accurately simulate the quadcopter's dynamics, the selected UAV, an unpowered DJI F450, was dropped six times on both a low-friction (UHMW PE) and on a high-friction surface (roofing shingles), as shown in Fig 6. The quadrotor was dropped from different heights on slopes ranging from 5° to 35°. Impact velocities were kept between 0.4 m/s and 1 m/s. The polycarbonate landing gear of the F450 was coated with Plasti-Dip. An electromagnet held the F450 horizontal before each drop. The drone's movements were recorded at 200 Hz using a motion capture system and filtered using a zero-phase 65-Hz low-pass Kaiser filter. GAs were used to identify eight parameters of the low-friction (LF) model using six drops, and to identify twelve parameters of the high-friction (HF) model using another six drops, as detailed in Table II. The leg weight ($m^\mathcal{C} g$ and $m^\mathcal{D} g$) and friction coefficient (μ_k) were measured in the LF model while the leg moment of inertia ($I_{yy}^{\mathcal{C}/\mathcal{C}_\text{CM}}$ and $I_{yy}^{\mathcal{D}/\mathcal{D}_\text{CM}}$) was calculated. The HF model was more sensitive to these parameters due to the rapid motion of the legs, so a better fit was obtained by adding these parameters to the GA.

To fit the parameters, the GA minimizes the average NRMSE between five of the simulated and measured states (i.e., x_B, z_B, $\dot{x}_B$, $\dot{z}_B$ and q_B) over the six drops for each surface type. Both GAs were run five times to validate the

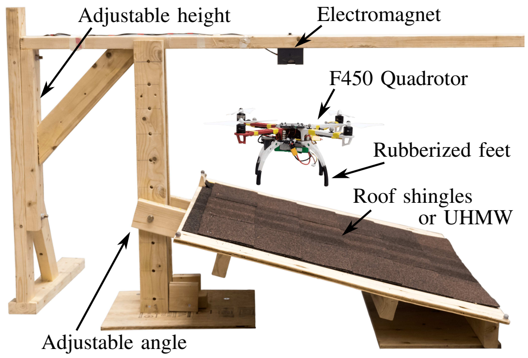

Fig. 6. Experimental setup for dropping the UAV on an inclined surface.

convergence. They were run with the same parameters as the GA used for the propulsion model, but with populations ranging from 400 to 800 individuals. For the LF surface, the five resulting NRMSEs varied between 8.3% and 12.1%. For the HF surface, they varied between 13.3% and 13.8%. Fig. 7 presents an example of the fitted states for the LF surface, and Table II lists the measured quadcopter's parameters and those obtained through the GAs. Slight differences between both models are possibly due to the plastic landing gears dynamically reacting differently to the different surfaces and to the asperities present in the roofing shingles.

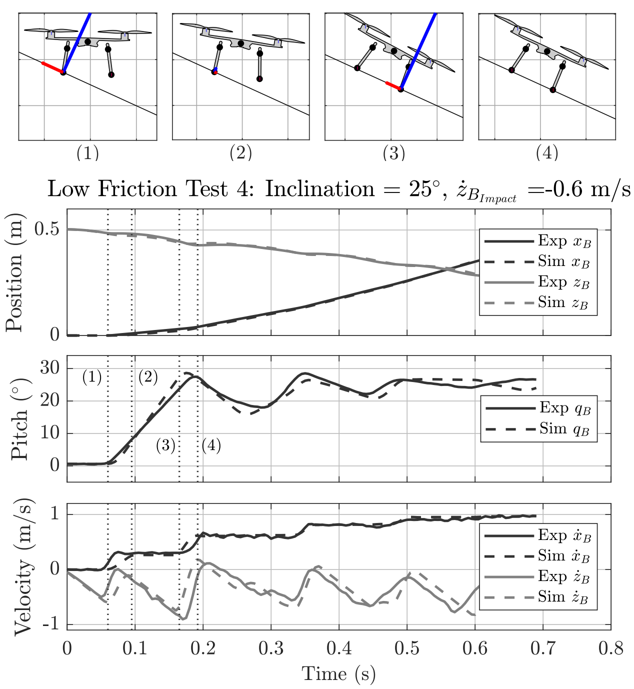

Fig. 7. UAV position (x_B, z_B), pitch (q_B), and velocity ($\dot{x}_B$, $\dot{z}_B$) obtained from landing experiments and simulations on the LF surface (bottom), and four simulated snapshots near the start of the drop (top). The normal contact force (blue) and the tangent friction force (red) are shown in the top figure. At (1), the rear leg contacts the ground and angular velocity rapidly augments. At (2), the rear leg leaves the ground and angular velocity remains high. At (3), the front leg impacts the ground, which acts to reduce the angular velocity of the UAV. At (4), the front leg leaves the ground. In this case, the quadrotor continues to bounce down the slope.

These results demonstrate that the model accurately predicts drone's behavior, allowing it to be used to develop different quadrotor landing control strategies.

TABLE II

DJI F450 MEASURED AND IDENTIFIED PHYSICAL PARAMETERS

Parameter	Measured	Low-friction GA mean ($\bar{x} \pm \sigma$)	High-friction GA mean ($\bar{x} \pm \sigma$)
$m^{\mathcal{B}}$ (kg)	1.242	—	—
$I_{yy}^{\mathcal{B}/\mathcal{B}_{\text{CM}}}$ (kg.m^2)	0.0137	—	—
dx_j (mm)	—	88±5	67±1
dz_j (mm)	—	24±8	19±7
dx_f (mm) [a]	105	—	—
dz_f (mm) [a]	151	—	—
k_h (N/m)	5600-6600[c]	6440±599	6670±350
b_h (N.s/m)	3.6-8.9[c]	14.3±4.6	20.3±1.3
k_t (N.m/rad)	14-16[c]	10.5±0.3	3.44±0.4
b_t (N.m.s/rad)	0.009-0.037[c]	0.056±0.045	0.017±0.005
k_s (N/m)	0.4e5-2.5e5[c]	1.10e5±0.07e5	1.49e5±0.1e5
b_s (N.s/m)	—	0.042±0.01	0.058±0.036
$m^{\mathcal{C}}$ (kg) [b]	0.02	—	0.015±0.004
$I_{yy}^{\mathcal{C}/\mathcal{C}_{\text{CM}}}$ (kg.m^2) [b]	2.0e-4	—	2.1e-4±1.7e-4
μ_k [b]	0.44	—	0.87±0.11
$\mu_s - \mu_k$	—	N/A	0.08±0.07

[a] Leg length h and "at rest" angle of legs q_n are calculated using the measured foot position and the joint position obtained by the GAs.
[b] These parameters were measured for the LF model, but were obtained in-situ using the GA for the HF model.
[c] These measured values were only obtained for validation of the GA results, using FEA modeling [12], contact modeling [17] and damping coefficient calculations [18].

III. CONTROL DESIGN AND RESULTS

Using the validated 2D simulation environment, multiple simple control algorithms were tested. Traditional multirotors try to remain horizontal during landing, which does not allow for landing on inclined surfaces. This section presents a basic landing control sequence to demonstrate the effectiveness of reverse thrust. Experimental trials were conducted to validate simulations in a wide range of conditions. Observations made during this process helped design an angular impulse controller to minimize bouncing after touchdown. This control method takes advantage of prior knowledge of the slope inclination and of the drone's touchdown velocity. Due to the fact that bounces occur rapidly (~100 ms) and that the rotor response time is of the same order of magnitude, a feedback controller would not efficiently react to the intermittent contacts. More complex feedforward algorithms could be used, but if the timing of the impacts or the model are off, more energy might possibly be injected into the system.

A. Reverse Thrust

To illustrate the benefits of reverse thrust, two landing methods were compared. The baseline method shuts off the motors when the inertial measurement unit (IMU) detects an impact. The other method simply applies maximum reverse thrust on all motors at impact to increase friction. This also reduces the bouncing amplitude, helping the quadrotor to quickly come to a stop.

These simple control sequences were tested in simulations over a range of slope angles (0° to 45°) and vertical impact speeds (0 to 2 m/s), on both the LF and HF surfaces. Instead of using the average parameters from Table II, these simulations were conducted five separate times using the five best sets of parameters from the GA for each surface type. These sets of parameters are those providing the lowest NRMSE of the last generation of each GA. Fig. 8 presents the average results as landing maps. The color gradient represents the probability of a certain outcome. The areas in green indicate successful landings within 45 cm of the initial impact location, equivalent to the landing distance provided by the experimental setup. In orange are the conditions where the quadrotor landed within 1 m. Two failure types were differentiated in the simulations. The gray area marked "**A**" represents the impact conditions leading to the drone flipping over within 1 m of the impact zone, whereas the white area marked "**B**" defines a failure type where the multirotor remained in motion beyond 1 m of the impact location.

As can be seen from the increase in the maximum slope inclination at which the drone can land, there are significant gains to using reverse thrust in the landing algorithm. Reverse thrust allows for faster landing over a large range of possible inclinations. However, even if the maximum slope inclination is nearly doubled, landing on an HF surface is more challenging. On this type of surface, the drone is subject to contacts of short duration in rapid succession instead of longer sliding contacts, resulting in less energy dissipation through friction. As shown in Fig. 8, the average time required for the drone to land and immobilize itself is twice as high for the HF surface than the LF surface. At high-impact velocities, the HF surface makes the drone more likely to flip over, which explains the larger **A** zone. In Fig. 8, the dashed line indicates the natural static limits of the quadrotor. Effectively, on the LF surface, the quadrotor will slide from rest if the surface inclination is over 22°. On the HF surface, the limit represents the inclination at which the quadrotor will tip over from rest (35°), which happens before sliding occurs. With reverse thrust, these limits are increased to 48° and 67° respectively. Further improvements are required to allow the UAV to land dynamically at such high limits. In addition, low power adhesion mechanisms, such as electroadhesion, switchable magnets, grippers or dry adhesives, could be activated after landing to remain on the surface after terminating reverse thrust.

B. *Experimental Results*

Over 240 validation landings were performed using the same experimental setup as for the model validation. The DJI F450 quadcopter was controlled using an Arduino Zero, an Adafruit Servo Shield, a Sparkfun Razor IMU (collecting data at 1 kHz and filtered using a third-order 30 Hz low-pass Butterworth filter), and an Xbee S1 to transmit data. The Arduino was programmed with a simple attitude control [19] to keep the quadcopter level during the descent. A 2g threshold, measured by the accelerometer, activates the chosen landing control when an impact occurs. The impact velocity was

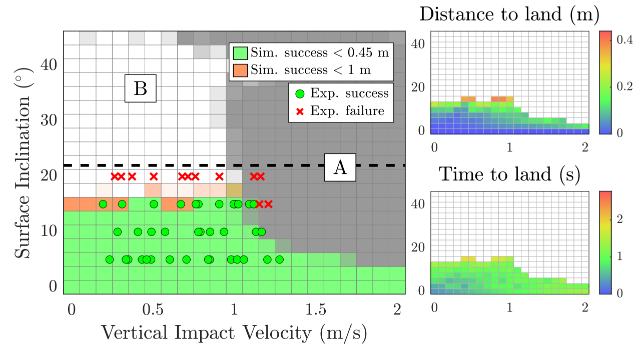

(a) Low-friction surface, 0% command at impact

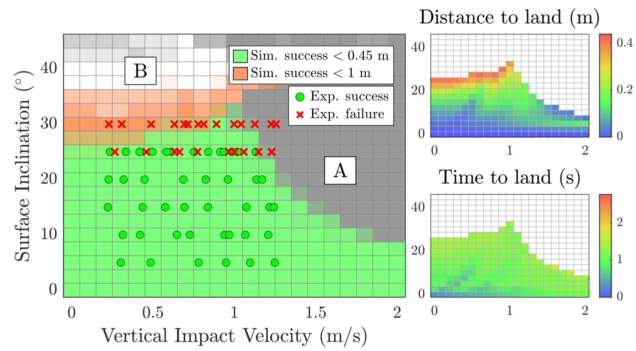

(b) Low-friction surface, -100% command at impact

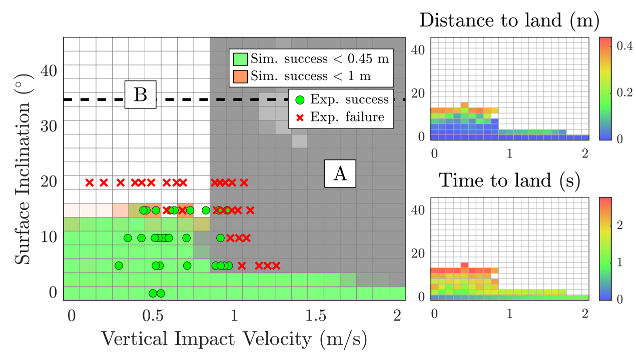

(c) High-friction surface, 0% command at impact

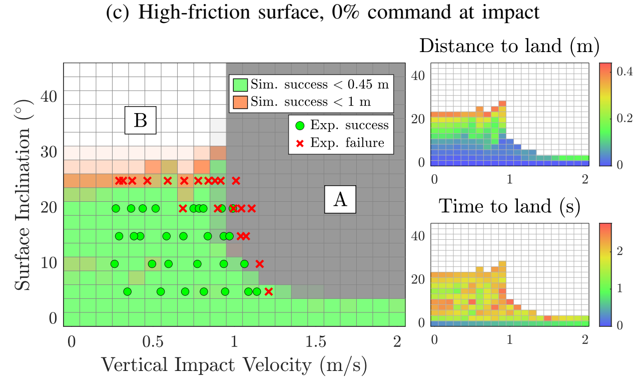

(d) High-friction surface, -100% command at impact

Fig. 8. Simulated landing maps for LF and HF surfaces, when shutting off the motors (0% command) and using full reverse thrust at touchdown (-100% command). Experimental landings are added to the maps and validate the simulations. The green area corresponds to successful landings within 45 cm of the initial impact, whereas the orange area denotes the conditions for a successful landing within 1 m. The gray **A** area signifies that the quadrotor flipped within 1 m of the impact location, whereas the white zone **B** corresponds to a "tumbling" failure. To the right of the maps are figures showing the distance and time required in simulation for the F450 to come to a rest. The dashed line represents the friction limit for the LF surface, whereas it represents the "tipping-over" limit for the HF surface.

recorded using a motion capture system. Landing successes and failures were added to the landing maps of Fig. 8. The drops were kept at under 1.2 m/s, because greater impact velocities would have likely broken the plastic landing gears. These experiments can be viewed in a supplementary video.[1]

The experimental results confirm the simulated performance of the controllers, as well as the accuracy of the dynamic model with the propulsion system. Furthermore, after the initial impact, the F450 went through roll and yaw rotations averaging about 19° and 27° respectively. This demonstrates that the simple model used remains valid to predict the quadrotor's landing envelope even under significant excursions from pure 2D conditions. Through simulation and experimental testing, it was observed that the rigid and undamped nature of the F450's landing gear limits the landing envelope. The suspension causes short duration contacts, providing less overall friction and damping to dissipate the system's energy.

C. Impulse Controller

As shown in Fig. 7, the angular velocity of the quadrotor increases after the impact with the rear leg until the front leg touches the ground. The high angular velocity at the second impact causes the quadrotor to either continue bouncing or tip over. This phenomenon is accentuated by the quadrotor landing gear's high rigidity and low damping. However, by using differential thrust, an angular impulse can be generated to eliminate the angular velocity. Using the knowledge of the surface's inclination and the predicted impact speed, a simple feedforward control can vary the timing and the duration of this angular impulse to eliminate the quadcopter's angular velocity and land parallel to the surface at the moment of the second impact (i.e., $q_B = q_A$ and $\dot{q}_B = 0$). Because of the critical timing, thrust reversal or complete motor shutdown is avoided. At impact, the motor commands are thus reduced to 10% and the impulse is generated at the desired time by sending a 80% command to the front motors. After the impulse is completed, both rotors are commanded to generate maximum reverse thrust to facilitate adhesion to the surface.

This approach was tested in the simulation environment, with the same ranges of vertical impact speed and slope inclinations as the previous simulations, on both types of surface. To find the optimum command, multiple combinations of impulse delay (time between impact and start of the impulse) and duration—ranging from 0 to 260 ms and 0 to 160 ms, respectively—were simulated for each combination of speed and slope angle. The impulse combination that minimized the angular velocity at the moment of the second impact was chosen. This procedure was again conducted for each of the five best sets of the F450's parameters for each surface type. The resulting average landing maps are presented in Fig. 9. This technique slightly increases the maximum inclination on which the quadrotor can land over a wider range of touchdown velocities. As expected, zone **A** is reduced, as tipping over occurs less frequently. Furthermore as shown by the black dashed boundary in Fig. 9, the use of reverse thrust is necessary to increase the landing envelope. Surprisingly, the impulse control alone only achieves comparable performance to the baseline control of Fig. 8(a) and 8(c). This could be explained by the linear impulse also created along the desired angular impulse to avoid thrust reversal. This pushes the drone away from the slope.

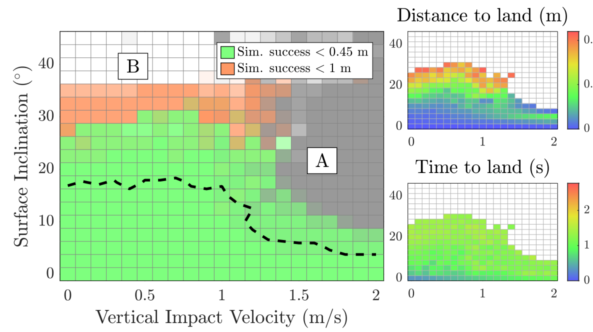

(a) Low-friction surface, impulse control

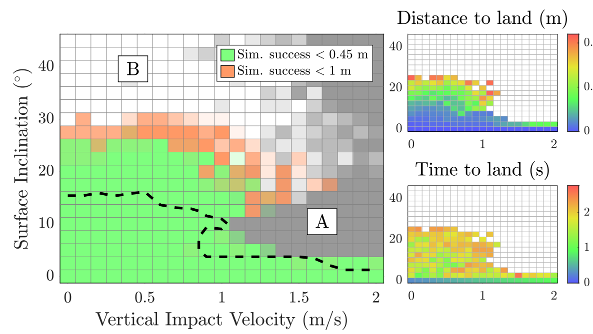

(b) High-friction surface, impulse control

Fig. 9. Simulated landing maps for LF (top) and HF (bottom) surfaces for landings using impulse control.

The obtained delay and duration of the impulse are displayed in Fig. 10. When landing on small inclinations at high speed, the controller chooses to omit the impulse and immediately generates reverse thrust on both motors after the impact, as seen in Fig. 10. In this region, the second impact occurs before the impulse is able to create a significant counter moment.

With ideal thrust reversal, a pure angular impulse could be generated, providing a more effective landing maneuver. This was simulated by eliminating the reversal delay of the model. The resulting landing maps are presented in Fig. 11. The faster thrust reversal extended the landing envelope considerably more than what the impulse with regular motors was able to achieve, while also shrinking the failure zone **A**. The time required to land also decreased, most notably for the HF surface, demonstrating that better motor reversal can contribute substantially to landing performance. Faster motor reversal could be implemented using sensored motors or variable pitch rotors [20].

IV. CONCLUSION

This paper evaluates the effectiveness of the use of bidirectional motors and reverse thrust to improve small multirotors'

[1] https://youtu.be/kjT5mfyiT4c

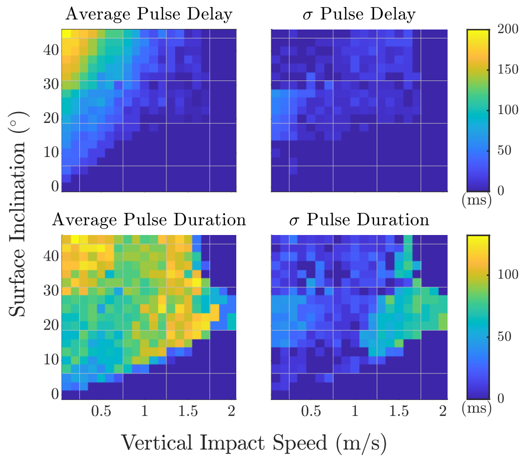

Fig. 10. Average pulse delay and its standard deviation (σ) between the five sets of simulations (top); average pulse duration and its standard deviation for the HF surface (bottom).

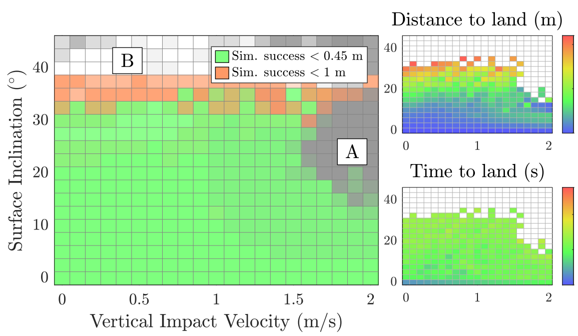

(a) Low-friction surface, fast impulse control

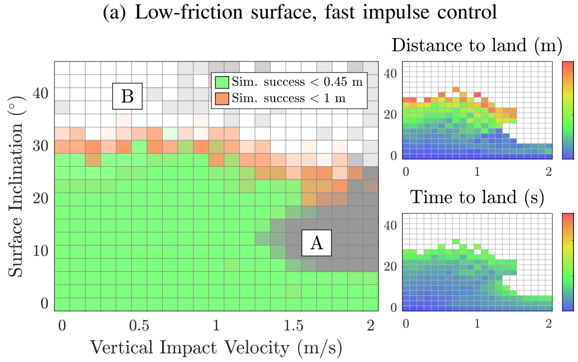

(b) High-friction surface, fast impulse control

Fig. 11. Simulated landing maps for LF (top) and HF (bottom) surfaces for landings using impulse control and faster motors.

ability to land on inclined surfaces. Through simulations and testing, we demonstrated that reverse thrust alone can increase the landing envelope of a small quadrotor by nearly doubling the maximum inclination on which it can land and by enabling high vertical velocity landings. This can be beneficial in situations where sudden disturbances are likely to occur (such as landing on roofs in the presence of wind). This result was achieved with a typical drone, and without adding any hardware. Using an angular impulse after the initial impact assisted the landing maneuver by eliminating undesired subsequent bounces. Furthermore, faster thrust reversal considerably increased the landing envelope.

Future work should include trials using the proposed solutions. The next steps involve implementing this landing strategy onto a small multirotor installed with a conventional autopilot and a sensor capable of measuring the inclination of a surface (such as an RGB-D camera). Outdoor trials could be conducted by landing the quadrotor on roofs. By using the designed model, parameters could also be adjusted to determine the rigidity and damping of ideal landing gears to minimize bouncing and tipping over. Finally, the proposed technique could be applied to landing on moving surfaces like the deck of a boat or a high-speed vehicle.

ACKNOWLEDGMENT

The authors would like to thank Marc-Antoine Leclerc and Frédéric Fafard for their help with trials.

REFERENCES

[1] DJI Support, "How to use DJI's return to home (RTH) safely," Aug 2017. [Online]. Available: https://store.dji.com/guides/how-to-use-the-djis-return-to-home/

[2] W. R. Roderick, *et al.*, "Touchdown to take-off: at the interface of flight and surface locomotion," *Interface focus*, vol. 7, no. 1, 2017.

[3] D. Mehanovic, *et al.*, "Autonomous thrust-assisted perching of a fixed-wing UAV on vertical surfaces," in *Conf. on Biomimetic and Biohybrid Systems*, 2017.

[4] A. Kalantari, *et al.*, "Autonomous perching and take-off on vertical walls for a quadrotor micro air vehicle," in *Proc. IEEE Int. Conf. Robot. Autom.*, 2015.

[5] J. Thomas, *et al.*, "Aggressive flight with quadrotors for perching on inclined surfaces," *J. of Mechanisms and Robotics*, vol. 8, no. 5, 2016.

[6] J. Dougherty, *et al.*, "Laser-based guidance of a quadrotor UAV for precise landing on an inclined surface," in *American Control Conference*, 2014.

[7] F. von Frankenberg and S. B. Nokleby, "Inclined landing testing of an omni-directional unmanned aerial vehicle," *Transactions of the Canadian Society for Mechanical Engineering*, vol. 42, no. 1, 2018.

[8] D. Brescianini and R. D'Andrea, "Design, modeling and control of an omni-directional aerial vehicle," in *Proc. IEEE Int. Conf. Robot. Autom.*, 2016.

[9] S. Park, *et al.*, "Design, modeling and control of omni-directional aerial robot," in *Proc. IEEE/RSJ Int. Conf. Intelligent Robots and Systems*, 2016.

[10] K. N. Mogensen, "Motor-control considerations for electronic speed control in drones," *Analog Applications J.*, 2016.

[11] W. Khan and M. Nahon, "Toward an accurate physics-based UAV thruster model," *IEEE/ASME Trans. Mechatron.*, vol. 18, no. 4, 2013.

[12] L. L. Howell, *Handbook of Compliant Mechanisms*. John Wiley & Sons, 2013.

[13] K. L. Johnson, *Contact Mechanics*. Cambridge University Press, 1987.

[14] P. C. Mitiguy and A. K. Banerjee, "Efficient simulation of motions involving coulomb friction," *J. of Guid. Control and Dynam.*, vol. 22, no. 1, 1999.

[15] H. Olsson, *et al.*, "Friction models and friction compensation," *Eur. J. Control*, vol. 4, no. 3, 1998.

[16] P. Mitiguy, *Advanced Dynamics and Motion Simulation*. Prodigy Press, 2014.

[17] L. Valentin and H. Popov, *Handbook of Contact Mechanics: Exact Solutions of Axisymmetric Contact Problems*. Springer-Verlag, 2019.

[18] JPE, "Structural damping properties of mechanical systems," 2020. [Online]. Available: https://www.jpe-innovations.com/page/precision-point/structural-damping-properties-mechanical-systems/

[19] D. Mellinger, *et al.*, "Trajectory generation and control for precise aggressive maneuvers with quadrotors," *Int. J. of Robot. Res.*, vol. 31, no. 5, 2012.

[20] M. Cutler, *et al.*, "Comparison of fixed and variable pitch actuators for agile quadrotors," in *AIAA Guidance, Navigation, and Control Conf.*, 2011.